

Influence of water uptake on the aerosol particle light scattering coefficients of the Central European aerosol

By PAUL ZIEGER^{1*†}, RAHEL FIERZ-SCHMIDHAUSER¹, LAURENT POULAIN², THOMAS MÜLLER², WOLFRAM BIRMILI², GERALD SPINDLER², ALFRED WIEDENSOHLER², URS BALTENSPERGER¹ and ERNEST WEINGARTNER^{1‡}, ¹*Paul Scherrer Institute, Laboratory of Atmospheric Chemistry, Villigen, Switzerland;* ²*Leibniz Institute for Tropospheric Research, Leipzig, Germany*

(Manuscript received 29 August 2013; in final form 14 February 2014)

ABSTRACT

The influence of aerosol water uptake on the aerosol particle light scattering was examined at the regional continental research site Melpitz, Germany. The scattering enhancement factor $f(\text{RH})$, defined as the aerosol particle scattering coefficient at a certain relative humidity (RH) divided by its dry value, was measured using a humidified nephelometer. The chemical composition and other microphysical properties were measured in parallel. $f(\text{RH})$ showed a strong variation, e.g. with values between 1.2 and 3.6 at $\text{RH} = 85\%$ and $\lambda = 550 \text{ nm}$. The chemical composition was found to be the main factor determining the magnitude of $f(\text{RH})$, since the magnitude of $f(\text{RH})$ clearly correlated with the inorganic mass fraction measured by an aerosol mass spectrometer (AMS). Hysteresis within the recorded humidograms was observed and explained by long-range transported sea salt. A closure study using Mie theory showed the consistency of the measured parameters.

Keywords: aerosol particle light scattering, hygroscopic growth, scattering enhancement, aerosol mass spectrometer, field measurements, optical closure study

1. Introduction

Atmospheric aerosol particles scatter and absorb solar radiation and thereby have an impact on the Earth's radiative budget (e.g. Haywood and Boucher, 2000; IPCC, 2007). Because aerosol particles can take up water, they can change in size and chemical composition depending on the ambient relative humidity (RH). This influences the direct aerosol radiative forcing, because the optical properties will change with varying RH (Pilinis et al., 1995). Therefore, long-term in-situ measurements (e.g. within monitoring networks) of optical and microphysical aerosol particle properties are usually performed at dry conditions to avoid the RH effect. For example, WMO/GAW (2003) recommends that aerosol in-situ measurements are performed at $\text{RH} < 40\%$. The RH dependency is especially important

for the particle light scattering coefficient σ_{sp} , which is defined within the Beer-Lambert law as the amount of radiation attenuated by the particles due to scattering (unit: m^{-1} ; see Liou, 2002). The dry measured in-situ values of σ_{sp} significantly differ from the ambient values, which are needed for climate forcing calculations. The knowledge on the RH dependency of σ_{sp} is also needed for the comparison or validation of aerosol remote sensing with in-situ measurements (see Ferrare et al., 1998; Voss et al., 2001; Zieger et al., 2011; Sheridan et al., 2012).

The key parameter to describe the RH dependency of σ_{sp} is called the scattering enhancement factor $f(\text{RH}, \lambda)$ which is defined as:

$$f(\text{RH}, \lambda) = \frac{\sigma_{\text{sp}}(\text{RH}, \lambda)}{\sigma_{\text{sp}}(\text{RH}_{\text{dry}}, \lambda)}, \quad (1)$$

where $\sigma_{\text{sp}}(\text{RH}, \lambda)$ is the aerosol particle light scattering coefficient at a certain wavelength λ and RH. $\sigma_{\text{sp}}(\text{RH}_{\text{dry}}, \lambda)$ is the corresponding scattering coefficient measured at dry conditions. $f(\text{RH}, \lambda)$ will typically increase with increasing RH and will be ≥ 1 , as long as the particles do not experience significant restructuring during water uptake.

*Corresponding author.

email: paul.zieger@itm.su.se

[†]Now at: Department of Applied Environmental Science, Stockholm University, Stockholm, Sweden

[‡]Now at: Institute for Aerosol and Sensor Technology, University of Applied Sciences, Windisch, Switzerland.

It depends on the chemical composition and on the size of the particle, which determines the scattering properties and the hygroscopicity. Several studies have measured and modelled $f(\text{RH}, \lambda)$ for different aerosol types: Marine and clean Arctic aerosols generally show a higher scattering enhancement (see Carrico et al., 2003; Zieger et al., 2010; Fierz-Schmidhauser et al., 2010b) than urban aerosols influenced by anthropogenic activities (McInnes et al., 1998; Zieger et al., 2011), continental aerosol particles (see Sheridan et al., 2001; Zieger et al., 2012) or mineral dust (Fierz-Schmidhauser et al., 2010a; Zieger et al., 2012). For example, in Ny-Ålesund, Spitsbergen, values of $f(\text{RH} = 85\%, 550 \text{ nm}) = 3.24 \pm 0.34$ (mean \pm standard deviation) were observed for Arctic and marine aerosol (Zieger et al., 2010), while the aerosol at the regional site in Cabauw, The Netherlands, showed values of $f(\text{RH} = 85\%, 550 \text{ nm}) \sim 1.4$ to 3.4 for urban polluted, continental and marine aerosol types (Zieger et al., 2011). Very low values of $f(\text{RH} = 85\%, 550 \text{ nm})$ were found for mineral dust dominated aerosol types, e.g. for long-range transported Saharan dust at the Jungfraujoch, Switzerland, with values around 1.0–1.2 (Fierz-Schmidhauser et al., 2010a; Zieger et al., 2012).

In this study, we present measurements of $f(\text{RH}, \lambda)$ together with comprehensive aerosol chemical, hygroscopicity and size distribution measurements at the Central European regional research station in Melpitz, Germany.

2. Measurement site

Field measurements were performed between February and March 2009 at the Central European research station in Melpitz, Germany (51°31′ 32″ N, 12°55′ 40″ E, 86 m a.s.l.), which is operated by the Leibniz Institute for Tropospheric Research (TROPOS). The site is surrounded by agricultural pastures, forests and small villages; the next largest cities are Leipzig located at about 50 km southwest and Torgau located about 5 km northeast of the site. Melpitz is part of the European Monitoring and Evaluation Programme (EMEP, Tørseth et al., 2012), the EU FP7 project Aerosols, Clouds, and Trace Gases Research InfraStructure Network (ACTRIS), and the German Ultrafine Aerosol Network (Birmili et al., 2009). Continuous aerosol measurements at Melpitz started in 1993, while aerosol scattering and absorption properties have been measured continuously since 2008. Several works (Spindler et al., 2010, 2012, 2013; Herrmann et al., 2006; Engler et al., 2007) give an overview on the size-segregated particle characterisation (PM_1 , $\text{PM}_{2.5}$, PM_{10} and particle number size distribution) at Melpitz and identify two very contrasting air mass origins: (1) air masses from westerly directions showing lower particle mass concentrations and (2) air masses from easterly directions with elevated particle mass concentrations due

to accumulation of particle mass during transport from continental and Eastern Europe.

3. Instrumentation

All particle in-situ instruments were connected to a common sampling line that sampled ambient air at 6 m above ground. The inlet consisted of a PM_{10} ambient size cut, allowing only particles with an aerodynamic diameter smaller than 10 μm to enter the sampling line. A regenerative diffusion dryer (Tuch et al., 2009) was used to keep the RH inside the sampling line below 30% in February/March 2009.

3.1. Light scattering measurements at dry and elevated RH

The aerosol particle light scattering coefficient σ_{sp} was measured at three distinct wavelengths ($\lambda = 450, 550, 700 \text{ nm}$) using an integrating nephelometer (DryNeph; TSI Inc., Model 3563). This instrument performed measurements always at dry conditions ($\text{RH} = 11.2 \pm 2.7\%$, mean \pm standard deviation during the campaign) and is used as a reference to the humidified nephelometer. The spectral course of the particle light scattering coefficient can be described by the Ångström formula:

$$\sigma_{\text{sp}}(\lambda) = \beta \lambda^{-\alpha_{\text{sp}}}, \quad (2)$$

where β is a particle concentration dependent coefficient, λ the wavelength of the light and α_{sp} the Ångström exponent of the particle light scattering coefficient. It reveals information on the particle number size distribution. For small values ($\alpha_{\text{sp}} \lesssim 1$) the particle number size distribution is dominated by supermicrometer particles, while for larger values ($\alpha_{\text{sp}} \gtrsim 1$) submicrometer particles are dominant.

The humidified nephelometer (WetNeph) measured σ_{sp} at controlled and elevated RH between approx. 30 and 90% at the same wavelengths as the DryNeph. The WetNeph was connected to the same inlet as the DryNeph and was operated in parallel to it. It is technically described in detail in Fierz-Schmidhauser et al. (2010c) and only a brief description will be given here. The atmospheric aerosol is directed with a flow rate of 10 lpm into a humidifier, in which the aerosol is exposed to RH up to approx. 89%, followed by a dryer that dries the aerosol particles continuously down to approx. 50% RH. If the humidifier and dryer are turned off, the RH decreases further to approx. 30%. This combined set-up allows measuring both branches of the hysteresis curve. The residence time from the humidifier to the nephelometer cell is typically 1–3 seconds. σ_{sp} is then measured in an integrating nephelometer of the same brand and model as the DryNeph (TSI Inc., Model 3563), however modified for a better temperature and humidity control.

The temperature and RH is measured at various points within the system using different sensors (Rotronic Hygro-ClipS) and a dew point mirror (Edge Tech, Model 2000 Dewprime DF). The uncertainty in the nephelometer measurements of the scattering coefficient (approx. 10%; Anderson et al., 1996) and the uncertainty of the RH inside the nephelometer cell (1–2%; Fierz-Schmidhauser et al., 2010c) contribute to the measurement uncertainty of $f(\text{RH})$. Both error sources combined give a relative uncertainty of $\Delta f(\text{RH} = 85\%) \approx 20\%$ for a very hygroscopic aerosol, which will decrease for less hygroscopic aerosol or smaller RH (and vice versa).

The WetNeph was set to measure in a constant RH mode for the first period of the campaign and set to measure in the humidogram mode for the second part of the campaign. A full humidogram (hydration and dehydration) took approximately 2 hours. The constant RH mode allows to better investigate the temporal evolution of $f(\text{RH})$, like diurnal cycles, while the humidogram mode characterises the shape of the $f(\text{RH})$ curve and reveals information on possible hysteresis behaviour.

The temperature of the two nephelometer systems was kept low (below approx. 23°C) to avoid losses due to the evaporation of ammonium nitrate (Bergin et al., 1997). The integration time of both nephelometers was set to 1 minute.

3.2. Hygroscopicity tandem differential mobility analyser

Hygroscopic particle growth factors were measured by a custom-built hygroscopicity tandem differential mobility analyser (H-TDMA). This instrument had been deployed for several years to characterise ambient aerosols (Massling et al., 2003), but was upgraded for continuous measurements at Melpitz during 2008 and 2009 according to the specifications outlined by Massling et al. (2011). During field operation, the H-TDMA was regularly checked for a correct particle sizing in the two differential mobility analysers. The H-TDMA performance was also verified by intermittent measurements of the hygroscopic growth factor of pure ammonium sulphate particles.

The H-TDMA allows the determination of the hygroscopic growth factor $g(\text{RH})$, which is defined as the diameter $D_{p,\text{wet}}$ at a certain elevated RH divided by its dry diameter $D_{p,\text{dry}}$:

$$g(\text{RH}) = \frac{D_{p,\text{wet}}(\text{RH})}{D_{p,\text{dry}}}. \quad (3)$$

$g(\text{RH})$ was measured at the dry diameters $D_{p,\text{dry}} = 50, 75, 110, 165, \text{ and } 265 \text{ nm}$ at $\text{RH} = 90\%$. The data for $D_{p,\text{dry}} = 165 \text{ nm}$ were not considered due to an instrumental error during the campaign. Growth factor probability density

functions were derived for each measurement using the TDMAin algorithm developed by Gysel et al. (2009). For this study, g was linearly interpolated for diameters in between the dry diameters and assumed to be constant with $g(D_{p,\text{dry}} = 50 \text{ nm})$ for particles smaller than the 50 nm and $g(D_{p,\text{dry}} = 265 \text{ nm})$ for particles larger than 265 nm.

Equation 3 can be parameterised using a one-parameter relationship which has been proposed, e.g. by Petters and Kreidenweis (2007):

$$g(a_w) = \left(1 + \kappa \frac{a_w}{1 - a_w} \right)^{\frac{1}{3}}, \quad (4)$$

where a_w is the water activity, which may be replaced by RH, if the Kelvin effect can be neglected. This is justified for larger particles, which are relevant for particle light scattering at the used wavelengths. The parameter κ characterises the average water uptake properties of a mixture of solutes (Raoult effect) and is a simple measure of the particle hygroscopicity.

The hygroscopic growth factor can also be calculated using the chemical composition measurements of multi-angle absorption photometer (MAAP) and aerosol mass spectrometer (AMS) (see Sections 3.3 and 3.5) of the different aerosol components and applying the Zdanovskii–Stokes–Robinson (ZSR) mixing rule (Stokes and Robinson, 1966). Black carbon (BC) is assumed to be insoluble ($g = 1$), while the value of g for the organic fraction was taken from Sjogren et al. (2008) who characterised the hygroscopic growth of aged organic aerosol (e.g. $g = 1.19$ for $D_{p,\text{dry}} = 100 \text{ nm}$ and $\text{RH} = 85\%$). The values of the retrieved salts and acids are taken from Topping et al. (2005). We refer to Fierz-Schmidhauser et al. (2010a); Gysel et al. (2007) for more details on the calculation and uncertainty.

3.3. Light absorption measurements

The aerosol particle light absorption was determined using a MAAP (Thermo Scientific Inc., Model 5012), which measures the light attenuation and backscattering of aerosols (at $\lambda = 637 \text{ nm}$, Müller et al., 2011) which are deposited on a filter. An internal radiative transfer code is applied to calculate the fraction of light absorbed by the deposited particles (Petzold and Schönlinner, 2004). The aerosol absorption coefficient σ_{ap} is retrieved by multiplying the reported BC concentration with the internal set value of the mass absorption cross-section of $6.6 \text{ m}^2 \text{ g}^{-1}$.

3.4. Number size distribution measurements

Particle number size distributions were measured by a dual mobility particle size spectrometer (custom-built by TROPOS and traditionally called TDMPS). The Melpitz TDMPS

(Birmili et al., 1999) consists of two mobility analysers covering a total particle size range of 3–800 nm (electrical mobility diameter), but was updated to circular sheath flow regulation according to the EUSAAR/ACTRIS recommendations (Wiedensohler et al., 2012). Multiple charge correction was performed according to Pfeifer et al. (2014).

The larger diameter size ranges were characterised using an optical particle size spectrometer (OPSS; Dust Monitor 1.108, Grimm GmbH). The OPSS determines the particle number size distribution (optical equivalent diameter) in 15 different channels between $D_p > 0.3 \mu\text{m}$ and $D_p > 20 \mu\text{m}$. It classifies the particles concerning their light scattering properties and uses light that is emitted from a laser diode at $\lambda = 780 \text{ nm}$. The OPSS is calibrated using polystyrene latex particles (PSLs). Since the refractive index of the atmospheric aerosol particles can differ from the PSL value, the particle number size distribution of the OPSS was corrected for different complex refractive index values (see e.g. Bukowiecki et al., 2011).

The measured particle number size distribution branches of TDMPS and OPSS were merged at $D_p = 800 \text{ nm}$ as the joint particle diameter channel. The first four OPSS channels were excluded with $D_p = 900 \text{ nm}$ being the first OPSS measured channel. The OPSS and TDMPS particle number size distributions agree well within the overlap region ($N_{\text{OPSS}}(350\text{--}725 \text{ nm}) = 0.93 * N_{\text{TDMPS}}(365\text{--}800 \text{ nm}) + 4.92$), $R^2 = 0.97$; R^2 : squared Pearson's correlation coefficient).

3.5. Chemical composition measurements

The chemical composition of the particles was characterised using an Aerodyne high resolution time-of-flight AMS (Aerodyne Research, U.S.A.). The instrument is described in detail e.g. in DeCarlo et al. (2006); Canagaratna et al. (2007). The AMS measures the chemical composition of non-refractory particles with diameters smaller than $1 \mu\text{m}$ (vacuum aerodynamic particle diameter). A collection efficiency of 0.5 was determined for the AMS using estimated mass concentrations from the TDMPS and the chemical analysis of filter samples Poulain et al. (2011).

A collection efficiency of 0.5 was determined for this AMS using the particle number size distribution and the chemical analysis of filter samples. Because soot, crustal material and sea-salts cannot be detected, the AMS is commonly considered to provide non-refractory PM_1 aerosol particle

chemical composition (Canagaratna et al., 2007). By combining the MAAP-based BC measurements and the AMS chemical composition, a highly time resolved and comprehensive picture of the submicron chemical particle composition can be provided. During 2008 and 2009, the same AMS was installed for different campaigns at Melpitz and the results are presented in Poulain et al. (2011), who also discuss the results of the AMS measurements performed during our time period in further detail.

In parallel to the AMS and MAAP measurements, aerosol particles were also collected by daily PM_{10} High Volume DIGITEL filter samples (Digitel Elektronik AG, Hegnau, Switzerland) from midnight to midnight. Filters were weighed to obtain concentrations of the total particle mass and water soluble inorganic cations and anions as well as OC/EC. Details on the different analytical methods and results for can be found in Spindler et al. (2010).

4. Calculation of optical properties

The particle light scattering enhancement was modelled using Mie theory with a computer code that is based on the work by Bohren and Huffman (2004). Further details on the Mie-based calculation of $f(\text{RH})$ can be found in Zieger et al. (2010). Spherical particles and a homogeneous internal mixture have to be assumed for the calculation. As an input, the measured particle number size distribution (see Section 3.4) and the complex particle refractive index are needed. The complex particle refractive index is derived from the chemical mass concentration measurements of the AMS and MAAP (see Sections 3.3 and 3.5). A volume weighted value is calculated using the particle refractive index and density values of the different components as given in Table 1 in Fierz-Schmidhauser et al. (2010a) in which similar calculations were performed. The imaginary part was neglected for all salt and organic components measured by the AMS and only BC, measured by the MAAP, contributed to the imaginary part of the refractive index.

5. Results

5.1. WetNeph analysis

The campaign at Melpitz was carried out from 23 February until 30 March 2009. The WetNeph was set to measure in

Table 1. Campaign average values of $f(\text{RH} = 85\%)$ for the different nephelometer wavelengths (λ : wavelength, STD: standard deviation, prctl: percentile)

λ	λ mean	STD	90th prctl.	75th prctl.	Median	25th prctl.	10th prctl.
450 nm	2.62	0.32	3.03	2.82	2.63	2.44	2.24
550 nm	2.77	0.37	3.25	3.02	2.78	2.56	2.34
700 nm	2.76	0.42	3.27	3.06	2.78	2.52	2.23

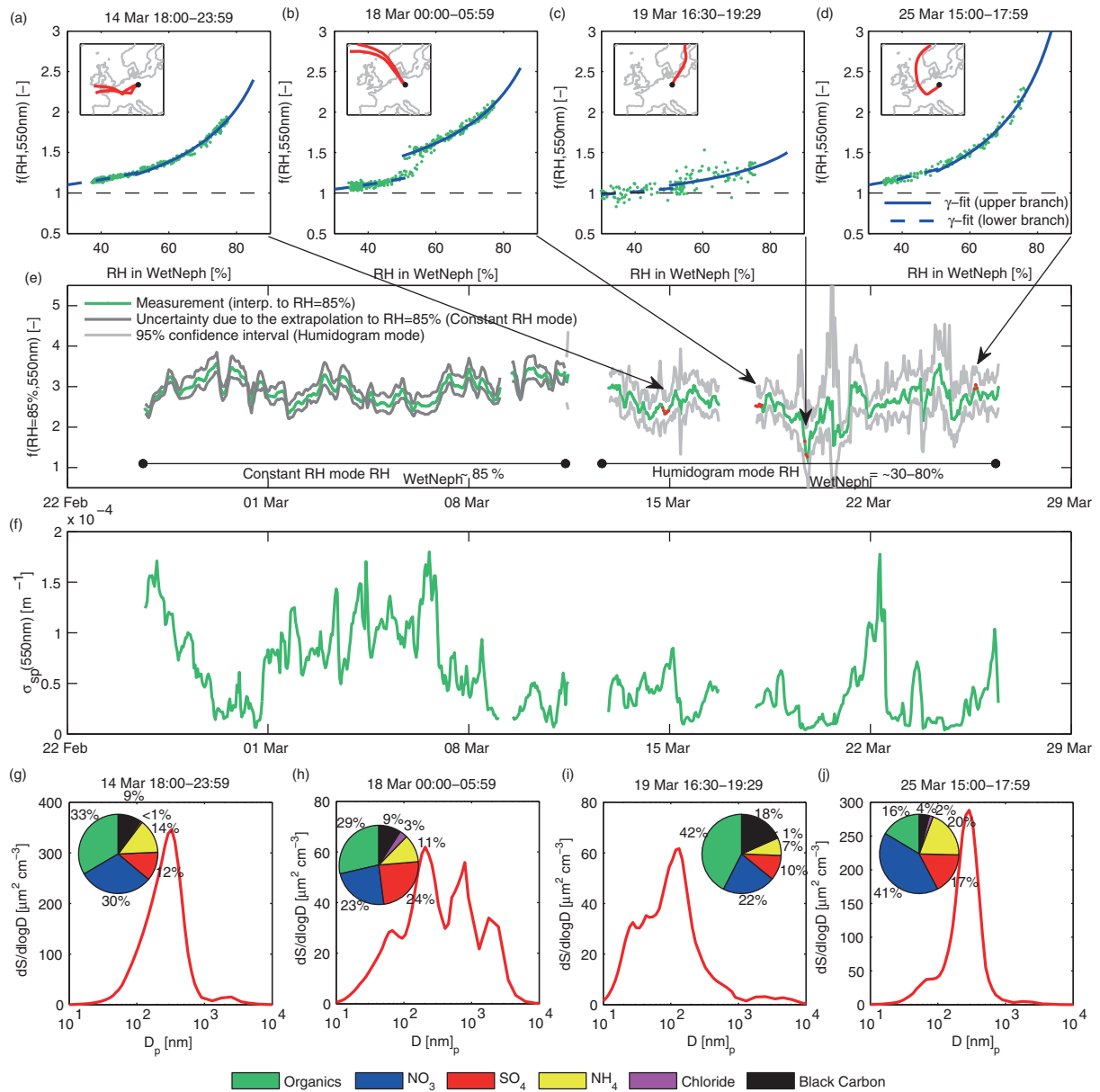


Fig. 1. Scattering enhancement $f(\text{RH})$ at $\lambda = 550 \text{ nm}$ measured at Melpitz. (a)–(d) Selected humidograms for different air masses (both hydration and dehydration scans; green points). The parameterisation of the upper and lower branch (γ -fit) is described in the text. Small inlays show 72-hour back trajectories for the specific time periods shown above the panel. (e) Time series of $f(\text{RH})$ at $\lambda = 550 \text{ nm}$ recalculated to $\text{RH} = 85\%$ (1-hour mean value). Indicated are the times when the WetNeph was measuring in the constant RH mode ($\text{RH} \approx 85\%$) or in the humidogram mode. Grey lines indicate the standard deviation (constant RH mode) or the 95% confidence interval (humidogram mode). The red marked points show the time periods for the humidograms shown in the upper panels. (f) Time series of the particle scattering coefficient σ_{sp} at $\lambda = 550 \text{ nm}$ measured at dry conditions (DryNeph). (g)–(j) Mean surface size distribution (TDMPS and OPC) and mean submicron chemical mass fraction (AMS and MAAP) for the same periods as the upper panels.

the *constant RH mode* for the first half of the campaign (24 February–11 March), while it measured *humidograms* (periodically changing RH) in the second half of the campaign (11–26 March). Example humidograms of $f(\text{RH})$ at $\lambda = 550 \text{ nm}$ are shown in Fig. 1a–d together with 72-hour air mass back trajectories (FLEXTRA, Stohl et al., 1995;

Stohl and Seibert, 1998) for the specific time periods. Shown are the hydration and dehydration scans of $f(\text{RH})$ (1 minute values, green points) together with a parameterisation of the upper and lower branch (see below). The particle surface size distribution measured by the TDMPS and by the OPSS as well as the mean submicron mass ratios

measured by the AMS and MAAP are shown for the same time periods in Fig. 1f–i. Figure 1a shows an example of westerly air masses with a smooth increase of $f(\text{RH})$ with increasing RH. The corresponding surface size distribution, which is generally relevant for the scattering properties, shows that the main contribution comes from particles in the fine mode at $D_p \approx 300$ nm, while the fine mode chemical composition is dominated by organics and NO_3 (Fig. 1g). The second example (Fig. 1b) shows almost no increase of $f(\text{RH})$ with increasing RH (hydration of the aerosol) until approx. 55% RH where $f(\text{RH})$ suddenly increases to about 1.5 and further rises with increasing RH. This deliquescence behaviour (sudden transition from the solid to the liquid state of the majority of the particle population) is attributed to transported sea salt, as can be seen in the back trajectories which indicate a transport of air from the North Sea towards Melpitz. In the dehydration mode (decreasing RH; max RH set in humidifier and drying the aerosol back to lower RH $\sim 50\%$), the deliquescence RH is passed and particles will become (partially) solid at a lower RH. This RH point (efflorescence) cannot be directly measured due to the limitations of the drying system, which only dries until approx. 50% RH. It should be mentioned that the observed deliquescence RH measured by the WetNeph is not identical with the thermodynamical deliquescence RH, since the particles are exposed to the highest RH in the humidifier and the RH decreases until the particle light scattering properties are measured inside the nephelometer (see Fierz-Schmidhauser et al., 2010c). The surface size distribution for the same period (Fig. 1h) clearly shows an increased coarse mode. As mentioned above, the AMS can only detect non-refractory material and thus cannot directly determine the sea salt contribution, although the chloride fraction in Fig. 1h is slightly enlarged compared to the other examples. Figure 1c shows a humidogram characterised by low values of $f(\text{RH})$, probably due to an increased influence of anthropogenic aerosol particles. This can be seen in the corresponding submicron mass ratio (Fig. 1i), where the BC and organic mass fraction make up approx. 60% of the total submicron mass. Additionally, the particle surface size distribution shows an increased contribution of Aitken mode particles ($D_p \approx 10$ – 100 nm), which is typical for fresh anthropogenic pollution. The humidogram in Fig. 1d shows a similar behaviour as Fig. 1a, but with an increased curvature and higher $f(\text{RH})$ values. The chemical composition reveals an increased nitrate fraction and less contribution from organics and BC, which are compared to NO_3 also less hygroscopic. The dominance of rather sharp mode at $D_p \approx 300$ nm characterises the particle surface size distribution as depicted in Fig. 1j.

The humidograms were parameterised using an empirical equation that has been used in previous studies (e.g. Clarke

et al., 2002; Carrico et al., 2003; Zieger et al., 2011) to describe the RH dependency of $f(\text{RH})$:

$$f(\text{RH}) = a(1 - \text{RH})^{-\gamma}, \quad (5)$$

where γ and a are two independent curve fitting parameters. The upper and lower branches were fitted separately (upper branch: humidifier at max. RH and dryer on, RH inside nephelometer $>55\%$; lower branch: dryer off and RH inside nephelometer $<50\%$). The result of this parameterisation is shown for the example humidograms in Fig. 1a–d.

The time series of $f(\text{RH})$ at 85% RH and $\lambda = 550$ nm is depicted in Fig. 1e together with the dry particle scattering coefficient in Fig. 1f. The humidograms were extrapolated to RH $\sim 85\%$ using eq. 5. During the constant RH mode, the RH inside the WetNeph was measured at $82.7 \pm 1.0\%$ (mean \pm standard deviation), with an average $f(\text{RH})$ of 2.69 ± 0.29 . The measured $f(\text{RH})$ values were extrapolated to RH = 85% by taking a constant value for a in eq. 5 ($a = 0.9 \pm 0.1$ at $\lambda = 550$ nm; mean and standard deviation of entire campaign). The resulting uncertainty from this extrapolation is seen in Fig. 1e as grey lines and is calculated by taking the upper and lower bounds of a (eq. 5). The uncertainty for the humidogram period is calculated by taking the upper and lower 95% confidence bounds for the fit parameters a and γ for the extrapolation to RH = 85%. Large uncertainties during the humidogram mode are mainly due to low concentrations and/or changing air masses during the 2-hour averaging time, which resulted in a higher fit-uncertainty (e.g. 20 March). The time series in Fig. 1e shows a high variability of $f(\text{RH})$ (see Table 1 with mean and percentile values of $f(\text{RH} = 85\%)$ for the entire campaign). A slight spectral dependency of $f(\text{RH})$ can be observed for the higher values (see 90th percentile values in Table 1); however, this difference is clearly below approx. 10% (at RH = 85%) and therefore the focus in the following discussion will be kept on the 550 nm wavelength. However, it should be mentioned that the wavelength dependency of $f(\text{RH})$ was reproduced and verified with Mie calculations using the measured size distribution and PM_{10} chemical composition (see Section 5.3).

The hysteresis behaviour in $f(\text{RH})$ is observed, when non-anthropogenic influenced sea salt with large fractions of sodium chloride was present. To illustrate the frequency of observed hysteresis, the difference of $f(\text{RH} = 55\%, 550 \text{ nm})$ of the upper branch minus the $f(\text{RH} = 55\%, 550 \text{ nm})$ of the lower branch is shown in Fig. 2 together with the sodium chloride (NaCl) mass fraction of the PM_{10} daily filter samples. An increased difference of the two $f(\text{RH})$ branches at RH = 55% corresponds to an increased NaCl mass concentration, which can be interpreted as a tracer for transported sea salt at Melpitz (Spindler et al., 2010). One particular sea salt transport event from the

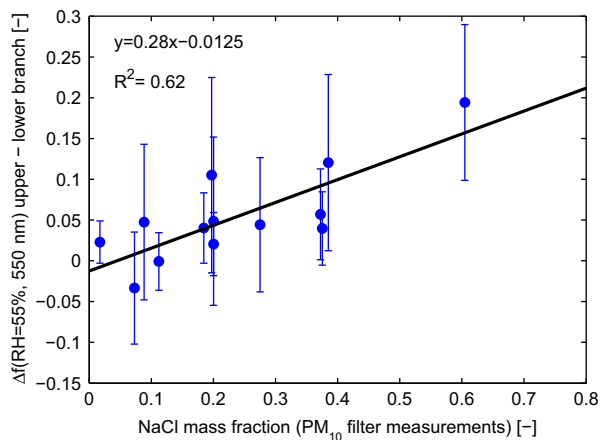


Fig. 2. $\Delta f(\text{RH} = 55\%, 550 \text{ nm})$ of upper and lower branch vs. the sodium chloride mass fraction of the filter measurements. The error bars denote the standard deviation of the daily mean values and the solid black line represents a linear regression.

Northern Sea was observed on 18 March 2009, which resulted in a clear hysteresis in the measured humidogram (see also humidogram and trajectories in Fig. 1b).

Figure 3a shows 72-hour air mass back trajectories colour-coded with the $f(\text{RH} = 85\%, 550 \text{ nm})$ measured at the time the air parcel arrived at the site, while Fig. 3b and 3c show the same trajectories but now colour-coded by the inorganic mass fraction determined by the AMS and MAAP measurements (see Section 5.2) and colour-coded by the mean surface area particle diameter measured by the TDMPS and OPSS. Westerly air masses dominated during the campaign. Increased values of $f(\text{RH} = 85\%, 550 \text{ nm})$ were connected to an increased inorganic particle mass fraction. Very low $f(\text{RH} = 85\%, 550 \text{ nm})$ values at approx. 1.1–1.2 were simultaneously measured with low inorganic particle mass fractions and small mean surface area particle

diameters, typically when the air arrived from north-east to Melpitz with a transport of accumulated anthropogenic air masses. In contrast to other sites (e.g. Jungfraujoch or Mace Head, see Fierz-Schmidhauser et al., 2010b; Zieger et al., 2012), no distinct dependency on large scale air mass transport phenomena or air mass sectors was observed at Melpitz and rather a high variability in $f(\text{RH} = 85\%, 550 \text{ nm})$ was characteristic for this site.

5.2. Chemical composition determining $f(\text{RH})$ at Melpitz

The colour-coded trajectories (Fig. 3) already point towards the fact that the scattering enhancement is mainly correlated with the inorganic mass fraction and is less dependent on the mean surface area particle diameter. The main chemical particle mass fractions versus $f(\text{RH} = 85\%, 550 \text{ nm})$ are shown in Fig. 4. They are calculated by dividing the individual particle mass concentrations of organic, nitrate, sulphate, ammonium (all measured by the AMS) and BC (measured by the MAAP) by the sum of all. The inorganic particle mass fraction is calculated by dividing the sum of nitrate, ammonia and sulphate concentration by the sum of all (incl. BC). Organics and BC mass fractions are clearly anti-correlated with $f(\text{RH} = 85\%, 550 \text{ nm})$ due to the lower hygroscopicity of these compounds, while inorganic substances clearly show a positive correlation with $f(\text{RH} = 85\%, 550 \text{ nm})$ due to their hygroscopic characteristics. The ammonium mass fraction shows a similar strong (positive) correlation ($R^2 = 0.64$) as the total inorganic mass fraction ($R^2 = 0.57$), while the individual nitrate and sulphate mass fractions are only weakly correlated with $f(\text{RH} = 85\%, 550 \text{ nm})$. This is mainly attributed to the fact that ammonium is the common ion of the two major salts (ammonium sulphate and ammonium nitrate) and can

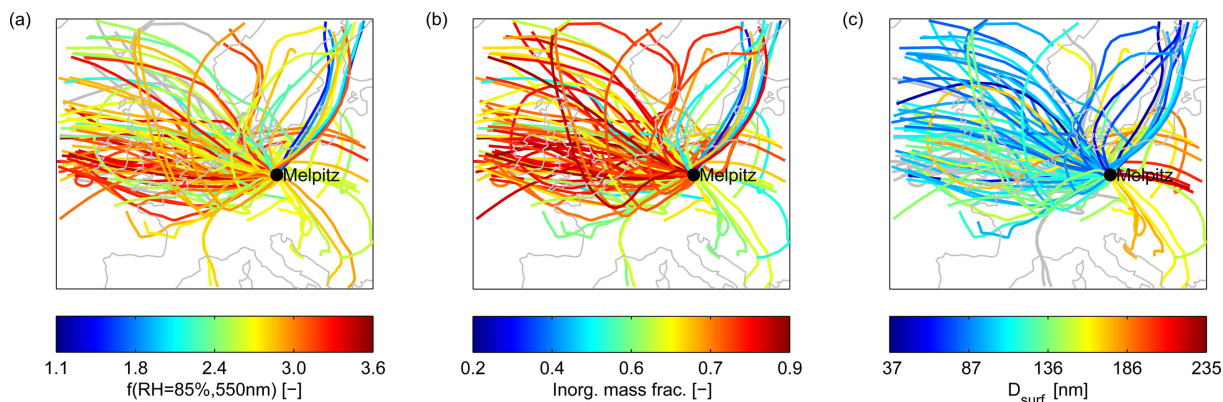


Fig. 3. FLEXTRA backward air trajectories (72 hours) for the entire measurement period colour-coded by different intensive aerosol parameters measured at the time the air parcel arrived at Melpitz, Germany (black dot): (a) Scattering enhancement $f(\text{RH} = 85\%, 550 \text{ nm})$; (b) Inorganic mass fraction; (c) Mean particle surface area diameter. The inorganic mass fraction is determined from AMS and MAAP measurements and represents a value for refractory and submicron particles only (see text for details).

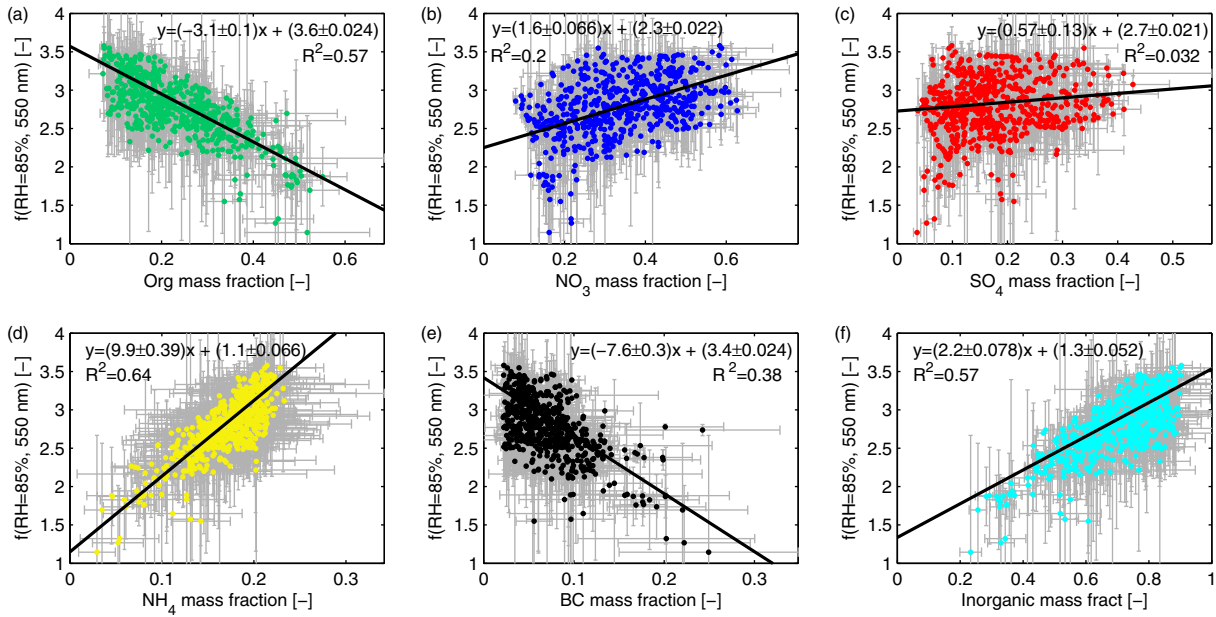


Fig. 4. Scattering enhancement $f(\text{RH} = 85\%, 550 \text{ nm})$ vs. different aerosol mass fractions measured by the AMS (sensitive for non-refractory and submicron particles only) and MAAp: (a) Organic mass fraction; (b) Nitrate mass fraction; (c) Sulphate mass fraction; (d) Ammonium mass fraction; (e) Black carbon (BC) mass fraction; (f) Inorganic mass fraction. The solid black line denotes a bivariate linear regression including weights and calculated uncertainties of slope and intercept.

be regarded as a proxy for the total inorganic content. Ammonium sulphate and ammonium nitrate also have different hygroscopic properties. The sum of the sulphate and nitrate mass fractions shows as expected a clear positive correlation with $f(\text{RH} = 85\%, 550 \text{ nm})$ (slope 2.9, $R^2 = 0.53$). Figure 4 clearly demonstrates that a (mean) particle chemical composition (e.g. the inorganic fraction) needs to be known to predict $f(\text{RH})$ at Melpitz. The orthogonal linear regressions were calculated according to York et al. (2004) by taking the error of the measurements into account, which allows retrieving an uncertainty of the slope and intercept given in Fig. 4. For the AMS and BC measurements, the standard deviation of the 1-hour averages was taken, while the uncertainty of $f(\text{RH} = 85\%, 550 \text{ nm})$ was calculated as described above. The $f(\text{RH})$ at a different RH can now be estimated from the chemical mass fractions using the equations in Fig. 4 together with eq. 5 and a fixed intercept of $a = 0.9$. However, one has to be aware that eq. 5 is a purely empirical equation with clear limitations for very low ($\text{RH} < 30\%$) or high ($\text{RH} > 90\%$) values of RH, because the upper and lower RH ranges were not covered by the measurements ($30 < \text{RH} < 90\%$). In addition, possible hysteresis effects (see Fig. 1b) are not captured using a fixed intercept and γ -value to calculate $f(\text{RH})$.

Figure 5 shows the squared correlation coefficient and the sign of the correlation of $f(\text{RH} = 85\%, 550 \text{ nm})$ with different in-situ aerosol particle parameters. As already seen above, the $f(\text{RH} = 85\%, 550 \text{ nm})$ is clearly correlated

with the inorganic mass fraction and anti-correlated with the organic mass fraction or the BC mass fraction. There is no significant correlation with any size parameters, such as the surface area concentration of the coarse mode fraction $S_{\text{CM}}/S_{\text{tot}}$ (measured by the OPSS and TDMPS), the total particle surface area fraction S_{tot} or the Ångström exponent of the particle light scattering coefficient at dry conditions (see eq. 2). This implies that the aerosol particle chemical composition (or at least a proxy of it) needs to be known to predict $f(\text{RH})$ from other continuous monitoring measurements. The rather weak correlation of the hygroscopic growth factor g with $f(\text{RH})$ ($R^2 = 0.2$) is most probably due to the short operation period of the H-TDMA and the fact the H-TDMA only measures at the dry diameters below 265 nm and therefore will not always cover all optically relevant size ranges such as a hygroscopic coarse mode, e.g. due to transported sea salt or non-hygroscopic mineral dust (Zieger et al., 2011).

5.3. Optical closure study

The different in-situ measurements were checked for consistency with respect to $f(\text{RH})$ and σ_{sp} by performing Mie calculations (see Section 4). As mentioned above, the correct OPSS sizing depends on the refractive index of the particles. The OPSS was calibrated by the manufacturer with PSL particles. However, the refractive index of PSL ($m_{\text{PSL}} = 1.586$) differs from the ambient aerosol values. In

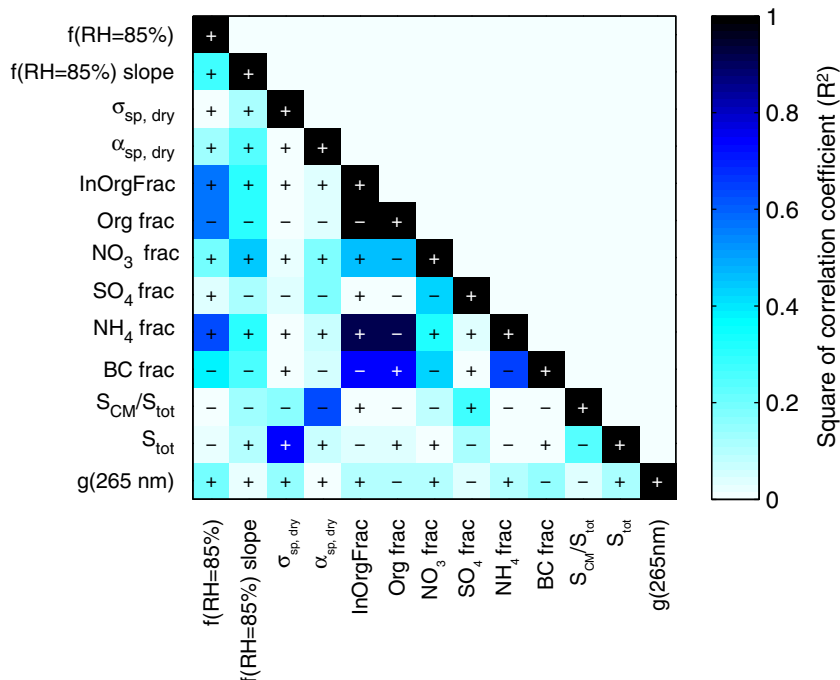


Fig. 5. Correlation plot of different aerosol parameters. $f(\text{RH}=85\%)$: scattering enhancement (at $\lambda = 550$ nm); spectral slope of $f(\text{RH}=85\%)$; $\sigma_{\text{sp,dry}}$: scattering coefficient (at $\lambda = 550$ nm); $\alpha_{\text{sp,dry}}$: Ångström exponent of dry particle light scattering coefficient; InOrgFrac: inorganic mass fraction; Org frac: organic mass fraction; NO_3 frac: nitrate mass fraction; SO_4 frac: sulphate mass fraction; NH_4 : ammonium mass fraction; BC frac: black carbon mass fraction; $S_{\text{CM}}/S_{\text{tot}}$: coarse mode surface area fraction; S_{tot} : aerosol total surface area; $g(265 \text{ nm})$: hygroscopic growth factor (from the H-TDMA) at the dry diameter of 265 nm. All mass fractions are determined from AMS and MAAP measurements (for non-refractory and submicron particles only).

particular, the imaginary part of m is usually not negligible. The particle number size distributions of the OPSS were therefore corrected by assuming the real part of the dry refractive index to be 1.5 (close to the value of ammonium sulphate and best found to fit with the number size distribution measurements of the TDMPS) and by changing the imaginary part between 0 and $0.02i$. This range is also supported by a recent analysis of long-term impactor measurements (Spindler et al., 2012). The refractive index m_{AMS} was retrieved from AMS and MAAP measurements (see Section 4) with $(m_{\text{AMS}}(550 \text{ nm})) = (1.54 \pm 0.0076) + (0.031 \pm 0.016)i$ (mean \pm standard deviation for entire campaign). The real part is close to the value of ammonium sulphate, while the imaginary part is close to the range estimated from the impactor measurements for the different size ranges (0.019–0.044*i*).

The Mie calculations were repeated for the particle light scattering coefficient at dry conditions and the comparison with the measured value (at $\lambda = 550$ nm) of the DryNeph is depicted in Fig. 6a. The centre points are the results for the OPSS correction with $m_{\text{OPSS}} = 1.5 + 0.01i$, while the error bars give the range of the calculated σ_{sp} for the other refractive indices and the non-corrected OPSS. The error bars in the x-direction give the standard deviation of the

1-hour mean values. The bivariate linear regression and the R^2 show a very good agreement with the DryNeph measurements and only a slight influence of the OPSS size distribution, showing the minor influence of the coarse particle fraction to the particle light scattering coefficient at the wavelengths used in this study and at this site. Figure 6b (lower row) shows the comparison as a box plot of the percentile difference between measured and predicted value ($100\% \times (\text{predicted}-\text{measured})/\text{measured}$). The central red mark in Fig. 6d is the median, the edges of the box are the 25th and 75th percentiles, the error bars show the extent to the most extreme data points that are not considered as outliers, while the outliers are plotted individually (red crosses). In addition, the number of points of the compared 1-hour averages is given. Fig. 6b reveals that the inter-quartile range of $\sigma_{\text{sp}}^{\text{dry}}$ can be calculated with a deviation of $< 10\%$ using the refractive index retrieved from the AMS and MAAP.

$f(\text{RH}=85\%, 550 \text{ nm})$ in Fig. 6b is also predicted using the hygroscopic growth factor and the refractive index derived from the AMS and MAAP measurements (see Sections 3.2 and 4). In addition, the $f(\text{RH}=85\%, 550 \text{ nm})$ is calculated using the hygroscopic growth factor of the H-TDMA (with less data points of the H-TDMA being

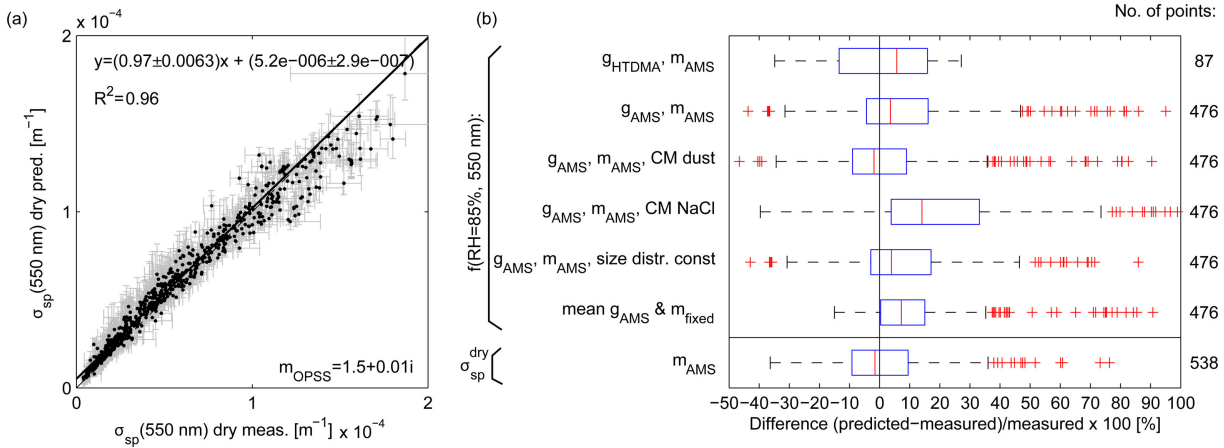


Fig. 6. (a) Predicted vs. measured scattering coefficient at dry conditions (at $\lambda = 550 \text{ nm}$). The error bars give the standard deviation of the measurements (x-axis) and the uncertainty of the calculated scattering coefficient due to the uncertainty in the OPSS (see text). (b) Box plots of the percentile difference between predicted and measured value. The upper six box plots are for the $f(\text{RH} = 85\%, 550 \text{ nm})$ for the different assumptions (see legend and text), the lower box gives the comparison for the dry scattering coefficient (OPSS not shifted, at $\lambda = 550 \text{ nm}$). The central red mark is the median, the edges of the box are the 25th and 75th percentiles, the error bars show the extent to the most extreme data points that are not considered as outliers, while the outliers are plotted individually (red crosses). The number of points is given on the right hand site (1-hour values). CM denotes the coarse mode which has been assumed to consist of sodium chloride (NaCl) or mineral dust.

available for our period) and the refractive index from the AMS and MAAP. g for $D_p > D_{p,dry}^{\text{max}}$ was assumed to be equivalent with g measured at the largest dry diameter $D_{p,dry}^{\text{max}}$ of the H-TDMA. Both predictions are compared to the measured values of the WetNeph. The result is seen in the first two rows of Fig. 6b (row 1: g from H-TDMA, row 2: g from AMS and MAAP). The calculated values were successfully predicted and lie within the same range as the measured ones; however, the comparison shows a moderate variability and small squared correlation coefficients $R^2 \sim 0.1-0.12$ (not shown). This can generally be explained by propagating uncertainties of the input parameters (e.g. the uncertainties in the combined size distribution) and in the assumptions of the Mie calculations (spherical particles, internal and homogeneous mixture). The interquartile range of $f(\text{RH})$ using g from the AMS or H-TDMA can be predicted with a deviation of $<15\%$, while the median of the percentile difference lies between 3 and 5%. The comparison to the H-TDMA measurements was influenced by the low number of measurement points during the observation period due to instrumental reasons, which probably explains the low R^2 value compared to similar calculations at other sites (e.g. Zieger et al., 2011).

To further investigate the sensitivity of the different input parameters, the Mie calculations were repeated with different assumptions (3rd to 6th row in Fig. 6b):

- (1) The coarse mode (CM; with $D_p > 1 \mu\text{m}$) was assumed to consist of mineral dust particles ($g = 1$ and m from Hess et al. (1998); Fig. 6b, row 3).

- (2) The CM was assumed to consist of pure sodium chloride particles (g and m were taken from the Seinfeld and Pandis (2006) and Topping et al. (2005); Fig. 6b, row 4).
- (3) The particle number size distribution was kept constant (mean value of TDMPS and OPSS of entire campaign; Fig. 6b, row 5).
- (4) A fixed value of $m = 1.5 + 0.005i$ and $g(\text{RH} = 85\%) = 1.53$ was assumed (mean value derived from AMS and MAAP measurements; Fig. 6b, row 6).

The first two assumptions on a pure NaCl or pure mineral dust particles were taken to test the extreme properties with highest and lowest known hygroscopicity for the coarse mode, knowing well that the coarse mode at Melpitz did not consist of pure NaCl. The interquartile range of $f(\text{RH})$ for the different scenarios can be predicted with a deviation of $<20\%$. Only the $f(\text{RH})$ with the coarse mode assumed to be of pure NaCl is clearly over-predicted with the interquartile range being above approx. 5–40%. As mentioned above, a pure NaCl coarse mode is rather unlikely and the daily measurements of the five-stage Berner impactors show a large contribution of organic matter, elemental carbon, nitrate, ammonia and undefined matter for the coarse mode (Spindler et al., 2012). A mean chemical composition together with the measured size distribution can be used to predict a mean $f(\text{RH})$; however, the variation of $f(\text{RH})$ will not be captured (see Section 5.2).

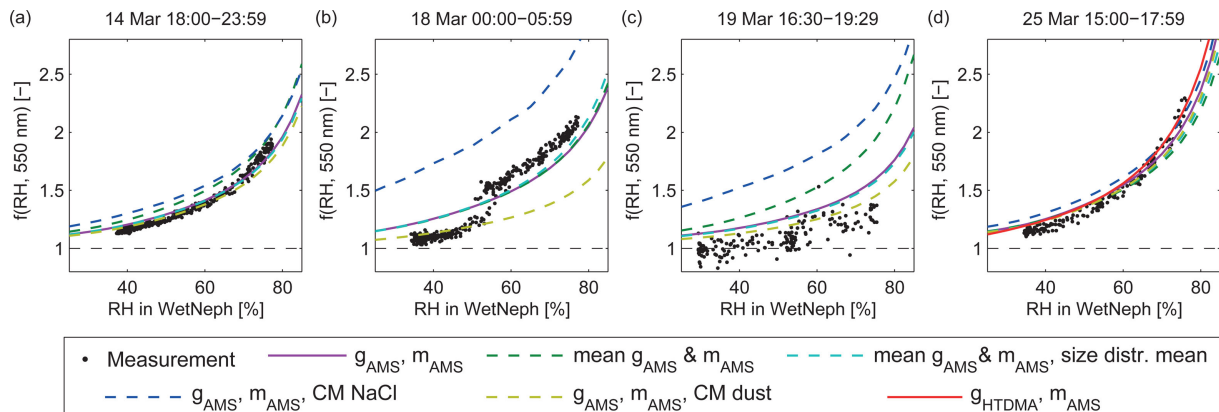


Fig. 7. (a)–(d) Measured and modelled $f(\text{RH})$ at $\lambda = 550$ nm for the example humidograms (see Figure 1) and the different model assumptions (see legend and text). CM denotes the coarse mode which has been assumed to consist of sodium chloride (NaCl) or mineral dust.

The closure results for the four example humidograms are shown separately in Fig. 7. It can be seen that the curvatures of $f(\text{RH})$ are well captured in almost all cases; however, substantial offsets and distinct artefacts occur for the different model assumption. This generally illustrates the limitations of the closure approach:

- (1) **The importance of the coarse mode.** The coarse mode clearly influenced $f(\text{RH})$ at Melpitz, as can be seen in the sea salt influenced humidogram (Fig. 7b). The chemical composition was only adequately determined by the AMS (and MAAP) for the fine mode, while assumptions had to be made for the coarse mode. Figure 7b therefore shows an overprediction for the NaCl and a clear underprediction for the mineral dust composed coarse mode (dashed blue and yellow curves). If the properties of the fine mode are extrapolated to the coarse mode, the result will also be an underprediction of $f(\text{RH})$. In addition, the particle number size distribution of the coarse mode was measured by an OPSS, which is limited in its resolution and correct sizing (see above). This is seen in Fig. 1h, where the particle surface size distribution is depicted for the same period. In fact, the clear anthropogenic influenced humidogram (Fig. 7c) also reveals a small increased coarse mode (see Fig. 1i), which explains the modelled differences between the NaCl and dust coarse mode cases (dashed blue and yellow curves in Fig. 7c).
- (2) **The assumption on an internally and homogeneously mixed aerosol.** This is crucial assumption, which is probably not fully appropriate for the aerosol encountered at Melpitz. The aerosol chemical composition, and with this the aerosol hygroscopicity and complex refractive index as model input parameters, will vary with particle size. In addition, only

the upper branch of the fully deliquescent aerosol can be modelled, which can lead to a clear overestimation of $f(\text{RH})$ at low relative humidities ($\text{RH} < 50\%$), when the aerosol is partially in the solid or liquid phase. This is clearly seen in Fig. 7b for the sea salt case, but may also be the reason for the slight overestimation of the predicted $f(\text{RH})$ for the other cases in Fig. 7 for $\text{RH} < 50\%$ for an externally mixed aerosol.

- (3) **Spherical particles.** Further limitations may result from the assumption of spherical particles, which has to be taken when optical particles are calculated by Mie theory. Sea salt and mineral dust, however, are not spherical and therefore Mie theory cannot be used (Nousiainen, 2009). Nevertheless, for measurements with an integrating nephelometer, the error in σ_{sp} is assumed to be $< 5\%$ for particles with $D_p < 1 \mu\text{m}$, but up to 30% for cubic particles $> 1 \mu\text{m}$ (Chamailard et al., 2003).

For the four cases shown in Fig. 7, the best agreement was achieved when the hygroscopic growth factor of the HTDMA was taken as an input parameter for the hygroscopic growth (red curve in Fig. 7d). The values of $g(\text{RH}) < 90\%$ were calculated by assuming a constant κ -value (eq. 4), which again may explain the slight overestimation at low RH since the κ -value will depend on RH (Petters and Kreidenweis, 2007). In general, all fine mode dominated humidograms were modelled with overall smaller differences between the different assumptions than for the coarse mode affected aerosol (see Fig. 7a and d vs. Fig. 7b and c).

We can conclude that the Mie calculations clearly show that the in-situ measurements are generally consistent, despite the large variation of the predicted $f(\text{RH})$, which can be explained by the uncertainty and limitations of the input data (e.g. PM_{10} size cut of AMS) and the assumptions

being made (spherical particles, internal and homogeneous mixture, etc.).

5.4. Context to previous studies

Continental and polluted air masses were also observed with the same WetNeph instrument at Cabauw, The Netherlands (Zieger et al., 2010) and at Mace Head, Ireland (Fierz-Schmidhauser et al., 2010b). Compared to these two sites, Melpitz had the unique opportunity to add highly time resolved aerosol chemical analysis of the AMS to the analysis of $f(\text{RH})$. At Cabauw, continental air masses coming from the east or the south had on average a value of $f(\text{RH} = 85\%, 550 \text{ nm}) = 1.86 \pm 0.17$ and 2.25 ± 0.16 , respectively (mean \pm standard deviation). In Mace Head, the air masses coming from the polluted (anthropogenic influenced) wind sector showed on average a value of $f(\text{RH} = 85\%, 550 \text{ nm}) = 1.8 \pm 0.26$. The $f(\text{RH} = 85\%, 550 \text{ nm})$ -ranges for maritime aerosol varied largely at Cabauw and Mace Head, ranging from 1.95 ± 0.14 for heavily polluted maritime aerosol to 3.38 ± 0.31 for pure maritime aerosol. The Melpitz retrieved value ($f(\text{RH} = 85\%, 550 \text{ nm}) \approx 2.5$) for the few maritime influenced periods would be included in this range. The comparison of $f(\text{RH})$ values of other studies is difficult to achieve due to very different instrumental set-ups, especially with respect to the applied particle size cuts (PM_{10} , PM_{10} or no size cut), different RH ranges or different wavelengths. While there are more studies that present $f(\text{RH})$ for marine, dust or strong anthropogenic influenced aerosol (see references above), only few suitable studies exist for continental aerosol types. However, Koloutsou-Vakakis et al. (2001) present $f(\text{RH})$ values from a continental site in the US (Bondville) with the same nephelometer type and also state a parameterisation to retrieve $f(\text{RH})$ at different RH which results in 1.58 for $\text{RH} = 85\%$ and $\lambda = 550 \text{ nm}$. This value is substantially lower than the measured average value here of 2.77 ± 0.37 for continental aerosol which could be explained by smaller particles or more hygroscopic particles (or a combination of both) encountered at Melpitz. The corresponding high inorganic mass fraction of the submicron refractory aerosol of 0.71 ± 0.13 supports this hypothesis. A minor but not negligible effect is the RH of the reference nephelometer. At Melpitz, the RH inside nephelometer was very low, with $\text{RH} = 11.2 \pm 2.7\%$ (mean \pm standard deviation during the entire campaign), while other studies often used $\text{RH} < 40\%$ as a reference since organic dominated aerosol particles already take up water at low RH. For example, Sjogren et al. (2007) retrieved a value of $g(40\%) = 1.05$ at the Jungfraujoch (Switzerland) which can cause an overestimation of the apparent dry scattering coefficient by approx. 10% which will propagate to the retrieved $f(\text{RH})$. Particle losses in the humidifier and systematic nephelometer offsets can be an additional source

for a systematic underestimation of $f(\text{RH})$. The achieved closure supports the values found here of $f(\text{RH})$, since they were reproduced from highly time resolved chemical and particle size distribution measurements. In general, particle size and chemical composition are both important for $f(\text{RH})$. In the Arctic for example, compensating effects of size and hygroscopicity were observed, e.g. small but less hygroscopic particles eventually had the same magnitude in $f(\text{RH})$ as large but more hygroscopic particles (like sea salt) with an average value of $f(\text{RH} = 85\%, 550 \text{ nm}) = 3.24 \pm 0.63$ (Zieger et al., 2010).

6. Conclusion

The influence of the water uptake on the aerosol particle light scattering coefficient has been investigated at the Central European regional research station Melpitz, Germany, using direct measurements of the scattering enhancement factor $f(\text{RH})$ by a humidified nephelometer system. In parallel, the chemical composition was measured by an AMS with a high time resolution. Other important aerosol parameters such as the particle number size distribution and the particle light absorption coefficient were measured as well. $f(\text{RH})$ has been found to be largely variable, e.g. with values between 1.2 and 3.6 at $\lambda = 550 \text{ nm}$ and $\text{RH} = 85\%$. Hysteresis was observed in the measured humidograms when sea salt was transported approx. 450 km from the North Sea to Melpitz. The chemical composition of PM_{10} was found to be the main factor determining the magnitude of $f(\text{RH})$, with a clear correlation to the inorganic mass fraction and an anti-correlation to the organic or BC mass fraction. $f(\text{RH})$ can be approximated using chemical composition measurements, if no direct measurements of $f(\text{RH})$ are available. A closure study revealed the consistency of all in-situ measurements.

7. Acknowledgements

This work was financially supported by the EC projects European Supersites for Atmospheric Aerosol Research (EUSAAR, contract 026140) and Global Earth Observation and Monitoring (GEOMON, contract 026140), as well as by the European Space Agency's Climate Change Initiative (aerosol_cci). P. Zieger was supported by a Post-Doc fellowship of the Swiss National Science Foundation (grant no. P300P2_147776). The aerosol measurements at Melpitz were supported by the European Integrated project on Aerosol Cloud Climate and Air Quality Interactions (EUCAARI), and the German Federal Environment Ministry (BMU) grant F&E 370343200 (German title: 'Erfassung der Zahl feiner und ultrafeiner Partikel in der Aussenluft'). NILU is greatly acknowledged for providing the FLEXTRA trajectories. We thank Friederike Kinder,

Nicole Niedermeier, and Andreas Massling (TROPOS) for their assistance with measuring and processing the H-TDMA data, as well as Thomas Tuch (TROPOS) for assistance with the measurement of the TDMPS data. We thank the anonymous reviewers for their helpful comments.

References

- Anderson, T., Covert, D., Marshall, S., Laucks, M., Charlson, R. and co-authors. 1996. Performance characteristics of a high-sensitivity, three-wavelength, total scatter/backscatter nephelometer. *J. Atmos. Ocean Tech.* **13**(5), 967–986.
- Bergin, M. H., Ogren, J. A., Schwartz, S. E. and McInnes, L. M. 1997. Evaporation of ammonium nitrate aerosol in a heated nephelometer: implications for field measurements. *Environ. Sci. Technol.* **31**(10), 2878–2883.
- Birmili, W., Stratmann, F., and Wiedensohler, A. 1999. Design of a DMA-based size spectrometer for a large particle size range and stable operation. *J. Aerosol Sci.* **30**, 549–553.
- Birmili, W., Weinhold, K., Nordmann, S., Wiedensohler, A., Spindler, G. and co-authors. 2009. Atmospheric aerosol measurements in the German Ultrafine Aerosol Network (GUAN): Part 1: soot and particle number concentration size distributions. *Gefahrst. Reinh. Luft.* **69**(4), 137–145.
- Bohren, C. and Huffman, D. 2004. *Absorption and Scattering of Light by Small Particles*. Wiley-VCH, Weinheim, Germany.
- Bukowiecki, N., Zieger, P., Weingartner, E., Jurányi, Z., Gysel, M. and co-authors. 2011. Ground-based and airborne in-situ measurements of the Eyjafjallajökull volcanic aerosol plume in Switzerland in spring 2010. *Atmos. Chem. Phys.* **11**(19), 10011–10030.
- Canagaratna, M., Jayne, J., Jimenez, J., Allan, J., Alfarra, M. and co-authors. 2007. Chemical and microphysical characterization of ambient aerosols with the Aerodyne aerosol mass spectrometer. *Mass Spectrom. Rev.* **26**(2), 185–222.
- Carrico, C., Kus, P., Rood, M., Quinn, P. and Bates, T. 2003. Mixtures of pollution, dust, sea salt, and volcanic aerosol during ACE-Asia: radiative properties as a function of relative humidity. *J. Geophys. Res.* **108**(D23), 8650.
- Chamaillard, K., Kleefeld, C., Jennings, S. G. and Ceburnis, D. 2003. Light backscattering and scattering by nonspherical sea-salt aerosols. *J. Quant. Spectrosc. Radiat. Transf.* **79**, 498–511.
- Clarke, A., Howell, S., Quinn, P., Bates, T., Ogren, J. and co-authors. 2002. Index aerosol: a comparison and summary of chemical, microphysical, and optical properties observed from land, ship, and aircraft. *J. Geophys. Res.* **107**(D19), INX2 32-1–INX2 32-3. doi: 10.1029/2001JD000572.
- DeCarlo, P., Kimmel, J., Trimborn, A., Northway, M., Jayne, J. and co-authors. 2006. Field-deployable, high-resolution, time-of-flight aerosol mass spectrometer. *Anal. Chem.* **78**(24), 8281–8289.
- Engler, C., Rose, D., Wehner, B., Wiedensohler, A., Brüggemann, E. and co-authors. 2007. Size distributions of non-volatile particle residuals ($d_p < 800$ nm) at a rural site in Germany and relation to air mass origin. *Atmos. Chem. Phys.* **7**(22), 5785–5802.
- Ferrare, R., Melfi, S., Whiteman, D., Evans, K. and Leifer, R. 1998. Raman lidar measurements of aerosol extinction and backscattering 1. Methods and comparisons. *J. Geophys. Res.* **103**(D16), 19663–19672.
- Fierz-Schmidhauser, R., Zieger, P., Gysel, M., Kammermann, L., DeCarlo, P. and co-authors. 2010a. Measured and predicted aerosol light scattering enhancement factors at the high alpine site Jungfraujoch. *Atmos. Chem. Phys.* **10**(5), 2319–2333.
- Fierz-Schmidhauser, R., Zieger, P., Vaishya, A., Monahan, C., Bialek, J. and co-authors. 2010b. Light scattering enhancement factors in the marine boundary layer (Mace Head, Ireland). *J. Geophys. Res.* **115**, D20204.
- Fierz-Schmidhauser, R., Zieger, P., Wehrle, G., Jefferson, A., Ogren, J. and co-authors. 2010c. Measurement of relative humidity dependent light scattering of aerosols. *Atmos. Meas. Tech.* **3**(1), 39–50.
- Gysel, M., Crosier, J., Topping, D. O., Whitehead, J. D., Bower, K. N. and co-authors. 2007. Closure study between chemical composition and hygroscopic growth of aerosol particles during TORCH2. *Atmos. Chem. Phys.* **7**(24), 6131–6144.
- Gysel, M., McFiggans, G. and Coe, H. 2009. Inversion of tandem differential mobility analyser (TDMA) measurements. *J. Aerosol Sci.* **40**(2), 134–151.
- Haywood, J. and Boucher, O. 2000. Estimates of the direct and indirect radiative forcing due to tropospheric aerosols: a review. *Rev. Geophys.* **38**(4), 513–543.
- Herrmann, H., Brüggemann, E., Franck, U., Gnauk, T., Löschau, G. and co-authors. 2006. A source study of PM in Saxony by size-segregated characterisation. *J. Atmos. Chem.* **55**(2), 103–130.
- Hess, M., Koepke, P. and Schult, I. 1998. Optical properties of aerosols and clouds: the software package OPAC. *Bull. Am. Meteorol. Soc.* **79**(5), 831–844.
- IPCC. 2007. *Climate Change 2007: The Physical Science Basis. Contribution of Working Group I to the Fourth Assessment Report of the Intergovernmental Panel on Climate Change*. Cambridge University Press, Cambridge, United Kingdom, London.
- Koloutsou-Vakakis, S., Carrico, C., Kus, P., Rood, M., Li, Z. and co-authors. 2001. Aerosol properties at a midlatitude northern hemisphere continental site. *J. Geophys. Res.* **106**(D3), 3019–3032.
- Liou, K. 2002. *An Introduction to Atmospheric Radiation*. 2nd ed, Vol. 84 of International Geophysics Series. Academic Press, San Diego, California, USA.
- Massling, A., Niedermeier, N., Hennig, T., Fors, E.O., Swietlicki, E. and co-authors. 2011. Results and recommendations from an intercomparison of six Hygroscopicity-TDMA systems. *Atmos. Meas. Tech.* **4**(3), 485–497.
- Massling, A., Wiedensohler, A., Busch, B., Neustüss, C., Quinn, P. and co-authors. 2003. Hygroscopic properties of different aerosol types over the Atlantic and Indian Oceans. *Atmos. Chem. Phys.* **3**(5), 1377–1397.
- McInnes, L., Bergin, M., Ogren, J. and Schwartz, S. 1998. Apportionment of light scattering and hygroscopic growth to aerosol composition. *Geophys. Res. Lett.* **25**(4), 513–516.
- Müller, T., Henzing, J., de Leeuw, G., Wiedensohler, A., Alastuey, A. and co-authors. 2011. Characterization and intercomparison

- of aerosol absorption photometers: result of two intercomparison workshops. *Atmos. Meas. Tech.* **4**(2), 245–268.
- Nousiainen, T. 2009. Optical modeling of mineral dust particles: a review. *J. Quant. Spectrosc. Radiat. Transf.* **110**(14–16), 1261–1279.
- Petters, M. and Kreidenweis, S. 2007. A single parameter representation of hygroscopic growth and cloud condensation nucleus activity. *Atmos. Chem. Phys.* **7**(8), 1961–1971.
- Petzold, A. and Schönlinner, M. 2004. Multi-angle absorption photometry—a new method for the measurement of aerosol light absorption and atmospheric black carbon. *J. Aerosol Sci.* **35**(4), 421–441.
- Pfeifer, S., Birmili, W., Schladitz, A., Müller, T., Nowak, A. and Wiedensohler, A. 2014. A fast and easy-to-implement inversion algorithm for mobility particle size spectrometers considering particle number size distribution information outside of the detection range. *Atmos. Meas. Tech.* **7**, 95–105.
- Pilinis, C., Pandis, S. and Seinfeld, J. 1995. Sensitivity of direct climate forcing by atmospheric aerosols to aerosol size and composition. *J. Geophys. Res.* **100**(D9), 18739–18754.
- Poulain, L., Spindler, G., Birmili, W., Plass-Dülmer, C., Wiedensohler, A. and co-authors. 2011. Seasonal and diurnal variations of particulate nitrate and organic matter at the IfT research station Melpitz. *Atmos. Chem. Phys.* **11**(24), 12579–12599.
- Seinfeld, J. and Pandis, S. 2006. *Atmospheric Chemistry and Physics: From Air Pollution to Climate Change*. John Wiley and Sons, Hoboken, NJ.
- Sheridan, P., Andrews, E., Ogren, J., Tackett, J. and Winker, D. 2012. Vertical profiles of aerosol optical properties over central Illinois and comparison with surface and satellite measurements. *Atmos. Chem. Phys.* **12**(23), 11695–11721.
- Sheridan, P., Delene, D. and Ogren, J. 2001. Four years of continuous surface aerosol measurements from the Department of Energy's Atmospheric Radiation measurement Program Southern Great Plains Cloud and Radiation Testbed site. *J. Geophys. Res.* **106**(D18), 20735–20747.
- Sjogren, S., Gysel, M., Weingartner, E., Alfarra, M., Duplissy, J. and co-authors. 2008. Hygroscopicity of the submicrometer aerosol at the high-alpine site Jungfraujoch, 3580 m a.s.l., Switzerland. *Atmos. Chem. Phys.* **8**(18), 5715–5729.
- Sjogren, S., Gysel, M., Weingartner, E., Baltensperger, U., Cubison, M. and co-authors. 2007. Hygroscopic growth and water uptake kinetics of two-phase aerosol particles consisting of ammonium sulfate, adipic and humic acid mixtures. *J. Aerosol Sci.* **38**(2), 157–171.
- Spindler, G., Brüggemann, E., Gnauk, T., Grüner, A., Müller, K. and co-authors. 2010. A four-year size-segregated characterization study of particles PM₁₀, PM_{2.5} and PM₁ depending on air mass origin at Melpitz. *Atmos. Environ.* **44**(2), 164–173.
- Spindler, G., Gnauk, T., Grüner, A., Iinuma, Y., Müller, K. and co-authors. 2012. Size-segregated characterization of PM₁₀ at the EMEP site Melpitz (Germany) using a five-stage impactor: a six year study. *J. Atmos. Chem.* **69**, 127–157.
- Spindler, G., Grüner, A., Müller, E., Schlimper, S. and Herrmann, H. 2013. Long-term size-segregated particle (PM₁₀, PM_{2.5}, PM₁) characterization study at Melpitz - influence of air mass inflow, weather conditions and season. *J. Atmos. Chem.* **70**, 165–195.
- Stohl, A. and Seibert, P. 1998. Accuracy of trajectories as determined from the conservation of meteorological tracers. *Q. J. Roy. Meteorol. Soc.* **124**(549), 1465–1484.
- Stohl, A., Wotawa, G., Seibert, P. and Kromp-Kolb, H. 1995. Interpolation errors in wind fields as a function of spatial and temporal resolution and their impact on different types of kinematic trajectories. *J. Appl. Meteorol.* **34**(10), 2149–2165.
- Stokes, R. and Robinson, R. 1966. Interactions in aqueous nonelectrolyte solutions. I. Solute–solvent equilibria. *J. Phys. Chem.* **70**(7), 2126–2131.
- Topping, D. O., McFiggans, G. B. and Coe, H. 2005. A curved multi-component aerosol hygroscopicity model framework: Part: inorganic compounds. *Atmos. Chem. Phys.* **5**(5), 1205–1222.
- Tørseth, K., Aas, W., Breivik, K., Fjærraa, A. M., Fiebig, M. and co-authors. 2012. Introduction to the European Monitoring and Evaluation Programme (EMEP) and observed atmospheric composition change during 1972–2009. *Atmos. Chem. Phys.* **12**(12), 5447–5481.
- Tuch, T., Haudek, A., Müller, T., Nowak, A., Wex, H. and co-authors. 2009. Design and performance of an automatic regenerating adsorption aerosol dryer for continuous operation at monitoring sites. *Atmos. Meas. Tech.* **2**(2), 417–422.
- Voss, K., Welton, E., Quinn, P., Frouin, R., Miller, M. and co-authors. 2001. Aerosol optical depth measurements during the Aerosols99 experiment. *J. Geophys. Res.* **106**(D18), 20821–20831.
- Wiedensohler, A., Birmili, W., Nowak, A., Sonntag, A., Weinhold, K. and co-authors. 2012. Mobility particle size spectrometers: harmonization of technical standards and data structure to facilitate high quality long-term observations of atmospheric particle number size distributions. *Atmos. Meas. Tech.* **5**(3), 657–685.
- WMO/GAW. 2003. *Aerosol Measurement Procedures Guidelines and Recommendations*. Report No. 153. World Meteorological Organization, Geneva, Switzerland.
- York, D., Evensen, N., Martínez, M. and Delgado, J. 2004. Unified equations for the slope, intercept, and standard errors of the best straight line. *Am. J. Phys.* **72**, 367–375.
- Zieger, P., Fierz-Schmidhauser, R., Gysel, M., Ström, J., Henne, S. and co-authors. 2010. Effects of relative humidity on aerosol light scattering in the Arctic. *Atmos. Chem. Phys.* **10**(8), 3875–3890.
- Zieger, P., Kienast-Sjögren, E., Starace, M., von Bismarck, J., Bukowiecki, N. and co-authors. 2012. Spatial variation of aerosol optical properties around the high-alpine site Jungfraujoch (3580 m a.s.l.). *Atmos. Chem. Phys.* **12**, 7231–7249.
- Zieger, P., Weingartner, E., Henzing, J., Moerman, M., de Leeuw, G. and co-authors. 2011. Comparison of ambient aerosol extinction coefficients obtained from in-situ, MAX-DOAS and LIDAR measurements at Cabauw. *Atmos. Chem. Phys.* **11**(6), 2603–2624.